Journal of Colloid and Interface Science 678 (2025) 218–225

Contents lists available at ScienceDirect

Journal of Colloid And Interface Science

journal homepage: www.elsevier.com/locate/jcis

Regular Article

Stress and flow inhomogeneity in shear-thickening suspensions

Esmaeel Moghimi*, Jeffrey S. Urbach, Daniel L. Blair

Department of Physics and Institute for Soft Matter Synthesis and Metrology, Georgetown University, Washington, DC, United States

GRAPHICAL ABSTRACT

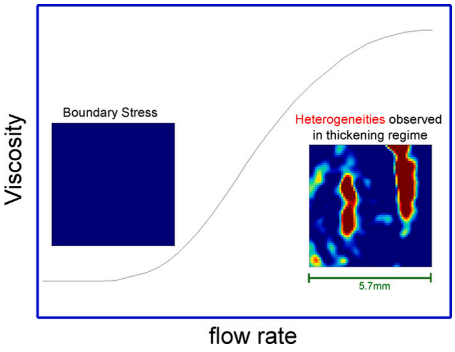

ARTICLE INFO

MSC:
0000
1111

Keywords:
Shear-thickening
Dense suspensions
Localized stresses
Nonaffine flow

ABSTRACT

Hypothesis: The viscosity of dense suspensions surges when the applied stress surpasses a material-specific critical threshold. There is growing evidence that the thickening transition involves non-uniform flow and stress with considerable spatiotemporal complexity. Nevertheless, it is anticipated that dense suspensions of calcium carbonate particles with purely repulsive interactions may not conform to this scenario, as indicated by local pressure measurements with millimeter spatial resolution.

Experiment: Here we utilize Boundary Stress Microscopy (BSM), a technique capable of resolving stresses down to the micron scale, to search for evidence of stress heterogeneity. In addition, we measure the flow field at the lower boundary of the suspension where the boundary stress is measured.

Findings: We find localized regions of high-stresses that are extended in the vorticity direction and propagate in the flow direction at a speed approximately half that of the rheometer's top plate. These high-stress regions proliferate with the applied stress accounting for the increased viscosity. Furthermore, the velocity of particles at the lower boundary of the suspension shows a significant and complex nonaffine flow that accompanies regions of high-stresses. Hence, our findings demonstrate that stress and flow inhomogeneity are intrinsic characteristics of shear-thickening suspensions, regardless of the nature of interparticle interactions.

---

* Corresponding author.
E-mail address: em1488@georgetown.edu (E. Moghimi).

https://doi.org/10.1016/j.jcis.2024.08.099
Received 27 March 2024; Received in revised form 7 August 2024; Accepted 13 August 2024

1. Introduction

Dense suspensions, when subjected to shear forces, exhibit a fascinating and intricate flow response known as shear thickening. This phenomenon manifests as a rise in viscosity, η, beyond a material-specific critical shear stress [1]. This behavior is of considerable importance in the engineering of fluids for a range of applications, encompassing body armor [2–4], medicine [5–7], and sensors [8,9]. As one notable example, in the formulation of protective gear, such as body armor and helmets, shear-thickening fluids are integrated to enhance impact resistance. These materials remain fluid under normal conditions but stiffen upon sudden impact, effectively dispersing and dissipating the energy, thus providing superior protection. As will be discussed in detail below, shear-thickening is profoundly influenced by particle concentration, the nature of interparticle forces and surface chemistry. At moderate particle concentrations, the suspension experiences continuous shear thickening (CST), characterized by a gradual increase in viscosity as the applied stress increases. However, at higher particle concentrations, the suspension has the potential to exhibit discontinuous shear thickening (DST), leading to a sudden and substantial increase in viscosity that may span several orders of magnitude.

While the concept of shear thickening has been acknowledged since the inception of suspension rheology, the detailed mechanisms driving it remain elusive. Nevertheless, a recent increase in research efforts has started to shed light on the fundamental aspects of this phenomenon [1]. A weak CST has been associated with the formation of particle clusters driven by hydrodynamic forces [10–12]. However, it turns out that lubrication forces are not sufficient to account for strong CST and DST [1]. Theoretical and simulation studies [1,13–15] supported by experimental findings [16,17] have shown that the dramatic increase of viscosity originates from a shift in interactions—from predominantly hydrodynamic interactions at low stress to predominantly frictional interactions—occurring when the stress reaches a level sufficient to surpass the repulsion between particles. Hence, shear thickening can be finely tuned by adjusting the particle roughness [18–22]. The proposed model effectively explains various aspects of the shear-thickening across a wide range of fluids that exhibit this behavior [23,16,24–26]. Despite this, fully grasping the complexity of shear thickening, including its spatiotemporal dynamics, remains a challenge.

Numerous experimental and computational studies have documented fluctuations in viscosity and shear rate [27–38] as well as nonaffine flows [28,39,38,40] within the shear-thickening regime. Recent velocity measurements conducted in the DST regime of cornstarch suspensions have revealed the presence of localized shear bands that propagate along the vorticity direction [41]. Moreover, density waves have been recognized in shear-thickening suspensions that propagate in the direction of flow [32]. By direct measurements of the spatially resolved stresses at the boundary of the sheared suspensions using boundary stress microscopy (BSM), we have observed localized regions of high stresses that emerge intermittently causing the viscosity to increase in the thickening regime. These localized stresses found to proliferate in the flow direction with the speed that is set by the rotational speed of the rheometer [35–38,40]. These large fluctuations in boundary stress are accompanied by dramatic fluctuations in suspension flow speeds [38,40]. Moreover, direct measurements of fluid migration indicated that the high-stress fronts are composed of a localized region of high dilatant pressure and low particle concentration [38]. In a recent work [42], the spatio-temporal variation of the normal stresses at the millimeter scale has been investigated for two shear-thickening fluids: a calcium carbonate suspension and a cornstarch suspension. The cornstarch suspension showed significant localized normal force fluctuations which propagate in the flow direction, very similar with shear stress fluctuations found from BSM. Conversely, in the calcium carbonate suspension, the local pressure was found to remain constant with time.

To gain further insights into the mechanism of shear-thickening in calcium carbonate suspensions, we evaluated localized shear stresses at the boundary using BSM. Notably, BSM offers a substantial advantage over pressure sensors employed in a prior reference [42] due to its high spatial resolution. With BSM, stresses can be resolved at the micrometer scale, which is approximately 10^{-3} times smaller than the spatial resolution achievable with the pressure sensors in Ref. [42]. Additionally, we probe the velocity of calcium carbonate suspensions at the boundary where local stress is measured. We find the appearance of localized regions of high stresses at the boundary in the shear thickening regime of calcium carbonate suspensions. These regions are extended in the vorticity direction and propagate in the flow direction with the speed which is nearly one-half the speed of the top plate. As the applied stress increases in the shear-thickening region, these high-stress regions become a larger fraction of the total surface area, accounting for the increased viscosity. Furthermore, we observe velocity fluctuations of particles at the boundary accompanying these high-stress regions. These findings unveil the existence of stress and flow heterogeneities at the boundary, which stands in contrast to the homogeneous normal stress reported by Ref. [42], yet aligns with prior observations in silica microspheres and non-Brownian cornstarch suspensions [35–38,40].

2. Materials and methods

The suspensions utilized in this study consisted of calcium carbonate particles (Eskal 500 from KSL Staubtechnik GmbH) dispersed in a mixture of water-glycerol (50-50 w/w%). Particles possess a rhomboidal-like shape and are moderately polydisperse with an average size of 4 μm [43,42]. To eliminate adhesive interactions between particles and induce purely frictional interactions with a short-range repulsive force, 0.05 w/w% of polyacrylic acid (PAA) was incorporated into the suspension [43]. For imaging calcium carbonate particles, 0.02M fluorescein sodium salt was added to the suspension.

Rheological experiments were carried out using an Anton Paar MCR 301 stress-controlled rheometer equipped with parallel-plate geometry (diameter of 25 mm and a 1 mm gap). The rheometer was integrated with an inverted Leica SP5 confocal microscope [44].

For BSM measurements, a layer of PDMS (Polydimethylsiloxane, Sylgard 184; Dow Corning) containing 2% curing agent was spin-coated onto glass cover slides with a diameter of 40 mm. The resulting film had a thickness of 50 ±3 μm. Subsequently, the slides underwent curing at 85 °C for 2 hours to ensure proper solidification of the PDMS layer. Following curing, the PDMS layer underwent a 40-minute functionalization process with 3-aminopropyl triethoxysilane (Fisher Scientific) through vapor deposition. For high-resolution BSM measurements, smaller sized (1 μm) carboxylate-modified fluorescent polystyrene (PS) beads were adhered to the PDMS surface. To image particles a 63× objective and a 145×145 μm^2 field of view was employed. To facilitate measurements at a lower magnification and thereby achieve a larger field of view, 10 μm PS beads were affixed to the PDMS surface. In this case, to prevent bead detachment during shearing, a second PDMS film was spin-coating on beads [35]. A 1.6× objective with the field of view $5.7 \times 5.7 mm^2$ was used to image these particles. In all experiments, the objective has been positioned approximately 4 mm away from the edge of the plate.

To determine the boundary stress, the deformation fields were initially evaluated using particle image velocimetry (PIV) with the PIVlab plugin in MATLAB. Subsequently, the boundary stresses were computed utilizing an extended traction force technique [45]. The spatio-temporal analysis of the flow component of the stress map was conducted by computing cross-correlation, $g(\vec{\delta r}, \delta t) = \langle \delta\sigma_x(\vec{r}, t)\delta\sigma_x(\vec{r} + \vec{\delta r}, t + \delta t)\rangle / \langle \delta\sigma_x(\vec{r}, t)^2\rangle$, averaged over $\vec{r}$ and t using the xcorr2 function in Matlab. The spatial autocorrelation ($\delta t = 0$) was also calculated in the same way. The profile of the spatial autocorrelation ($g(x)$, Fig. 4B) and spatiotemporal cross correlations (Fig. 4C) along the flow direction are computed by averaging over the middle 3 rows of pixels in the vorticity direction. The flow field of calcium carbonate particles at the bottom boundary was measured using PIV. To effectively capture fast flows in

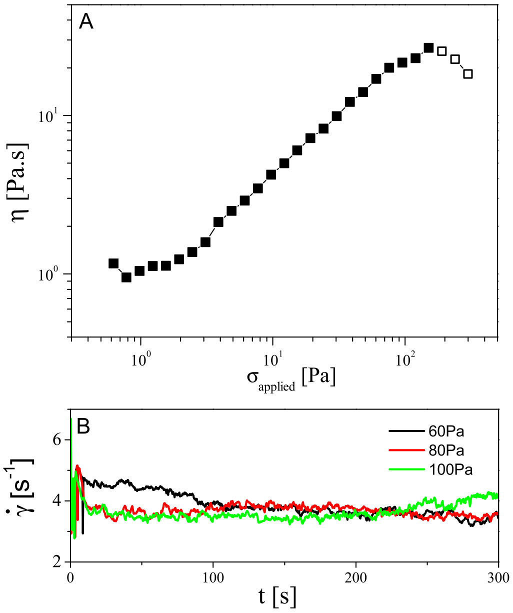

Fig. 1. Bulk Rheology of Calcium carbonate suspensions with $\phi = 54\%$. (A) Flow curve (Viscosity vs. rheometer shear stress). (B) Shear rate vs. time at different applied stresses.

the thickening regime, imaging was constrained to 128x512 pixels, consequently boosting the frame rate to 100 frames/s.

3. Results

3.1. Bulk rheology

As outlined in the materials and methods section, addition of polyacrylic acid (PAA) into a suspension containing calcium carbonate particles dispersed in a water-glycerol mixture results in the elimination of adhesive contacts between particles. This transformation yields a system of hard particles exhibiting purely frictional interactions with a short-range repulsive force [43]. The rheological behavior of these suspensions under increasing stress aligns with the shear-thickening phenomenon previously reported [46,23].

Fig. 1A shows the average viscosity, η, plotted against the stepwise increasing applied shear stress σ (flow curve) for the examined suspension at a volume fraction of $\phi = 54\%$. The flow curve shows a low-viscosity Newtonian plateau followed by shear thickening beyond the critical shear stress $\sigma_c \approx 2Pa$. Finally, at high shear stresses, $\sigma \geq 200Pa$, the viscosity experiences a slight decrease associated with sample fracture [43,42]. In this regime, we observe that the sample is dislodged from the rheometer plates. Fig. 1B shows examples of the shear rate measured by the rheometer as a function of time in the shear-thickening regime under constant applied stress. Within this regime, upon application of stress, the shear rate exhibits a transient increase before reaching a steady-state value. The steady state values of shear rate are nearly the same for different applied stresses. An intriguing observation is that, unlike dense cornstarch or silica suspensions [35,36,38], the shear in this case does not display appreciable intermittent fluctuations.

3.2. Boundary stresses

Alongside monitoring the bulk viscosity, we employ BSM to measure the boundary stresses exerted on the bottom plate of the rheometer. In BSM, micron-sized PS beads are chemically bonded to an elastic film made of PDMS with known thickness and modulus. Subsequently, the film is affixed to a cover glass, which serves as the bottom plate of the rheometer. The displacements of these beads are then probed using confocal microscopy to acquire the deformation field, enabling the calculation of the stress map at the boundary (see Methods).

Fig. 2A shows examples of the spatial map of the boundary stress component in the flow direction for different values of stress well inside the shear-thickening regime. The map encompasses an area of $5.7 \times 5.7mm^2$ and is captured at approximately 4 mm away from the edge of the plate. The maps are selected for instances when the localized stresses are at their peak, as indicated by arrows in Fig. 2B. The stress maps reveal distinct regions of elevated boundary stress that extend in the vorticity direction and propagate in the flow direction (Movie S1). The contribution of these high-stress regions to overall stress is determined by $\sigma_H = \sum \sigma_x(\vec{r}_i)/N$ where the sum is computed over all the positions $\vec{r}_i$ that satisfy the condition that $\sigma_x(\vec{r}_i) > 200Pa$ and $N = 3721$ is all the positions within the frame. The choice of the $200Pa$ cutoff for σ_H is based on the color map for the boundary stresses shown in Fig. 2A, where we observe that high-stress regions primarily appear for $\sigma_H > 200Pa$. This value is significantly higher than the maximum stress recorded in the low stress regions, including both signal and noise.

Fig. 2B shows time variations of σ_H for different values of applied stress. In contrast to the shear rate measured by rheometer, which does not show intermittent fluctuations, σ_H exhibits significant fluctuations whose frequency increases as the applied stress increases, similar to previous observations in measurements of dense cornstarch or silica suspensions [35,36,38]. The constant shear rate measured by the rheometer indicates that the average stress across the entire bottom boundary remains constant. Our measurements focus on local stress at the boundary; therefore, when we do not detect high-stress regions, they must exist in parts of the bottom boundary outside our measurement area at that time. If the averaged stress across the entire bottom boundary were fluctuating, we would expect to see corresponding fluctuations in the shear rate recorded by the rheometer.

In Fig. 3, we show the averaged values of stress within high stress regions alongside with their area fraction for different values of applied stress. As shown in Fig. 3 (black squares), the averaged values of stress within high stress regions do not change with the applied stress. However, the high stress regions proliferate as applied stress is increased (also evident from Fig. 2B) which accounts for the rapid rise in suspension viscosity, similar to our previous measurements of dense cornstarch or silica suspensions [35,36,38].

3.3. The propagation speed of high-stress regions

Next, we investigate the spatio-temporal evolution of these high-stress regions. The formation and dynamics of these regions appear stochastic, yet with evident translational motion in the flow direction (see Movie S1). An example of this motion is depicted in snapshots presented in Fig. 4A, where two high-stress regions traverse the field of view in the flow direction. The propagation speed and extent of these high-stress regions can be quantified by calculating the spatiotemporal cross-correlation of the boundary stress (see Methods). In Fig. 4B, we compare the spatial autocorrelation of high-stress regions along the flow direction under various applied stresses. The autocorrelation curves at different stress levels reveal a weak second peak, representing the average distance between two neighboring high-stress regions, approximately 2-3 mm. With increasing applied stress, the second peak occurs at slightly larger distances. The propagation speed of these high-stress regions can be determined by evaluating their cross-correlation at various delay times (see Methods). As an example, in Fig. 4C, we illustrate cross-correlations $g(\vec{\delta r}, \delta t)$ in the direction of flow at different time intervals for an applied stress of 100 Pa. The reduction in the amplitude of the peak of $g(\vec{\delta r}, \delta t)$ with increasing time interval is a result of the propagation and disappearance of high-stress regions, with the peak shifting towards larger distances indicating a net motion in the direction of flow. The average propagation speed is subsequently computed from the shift of the peak of $g(\vec{\delta r}, \delta t)$ with delay time (inset). The findings indicate that the high-stress regions propagate in the flow direction at a speed approx-

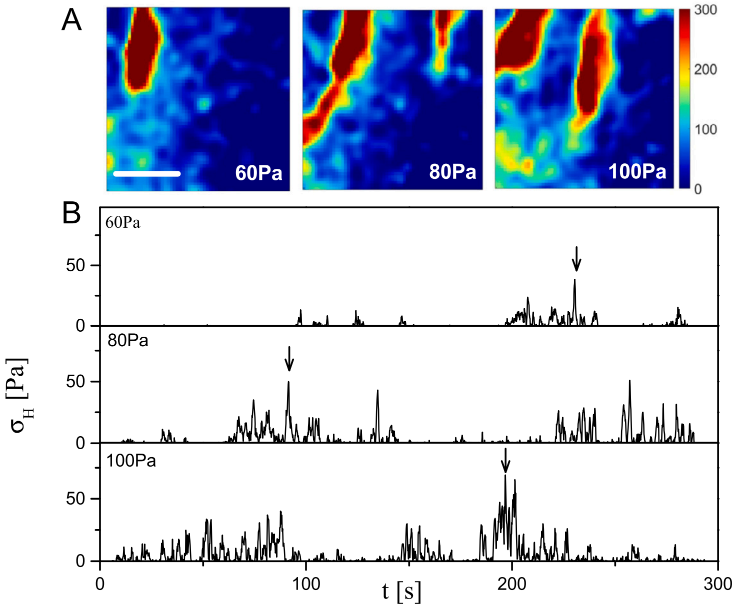

Fig. 2. BSM measurements in the shear thickening regime. (A) Snapshots of the boundary stress map in the flow direction (σ_x) captured at the peak of the local stress (indicated by arrows in B) for $\sigma_{applied}$ =60, 80 and 100 Pa (Scale bar: 2 mm). (B) Time series of stress contribution arising from high stresses (regions where $\sigma_x(\vec{r}_i) > 200 Pa$).

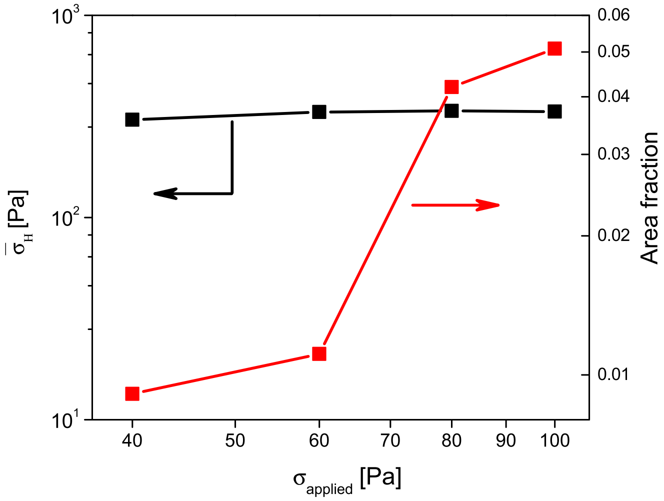

Fig. 3. The average stress within high-stress regions (dark squares, left vertical axis) and the area fraction of the stress maps containing these high stresses (red squares, right vertical axis) vs. the applied stress.

imately one-half that of the rheometer's top plate (Fig. 4D), resembling the behavior observed in suspensions of silica particles [35–37,40].

4. Concurrent measurements of boundary stress and flow field

By integrating rheology with high-speed confocal microscopy, we can directly examine the flow field within regions experiencing high stresses [44]. In this context, a high magnification objective (63×) with a field of view $145 \times 145\ \mu m^2$ is employed, resulting in a substantial improvement in the resolution of the stress signal derived from BSM. To enhance visibility, fluorescein sodium salt is introduced into the solvent, enabling a distinct visualization of the suspension bottom layer (see Movie S2). The significant refractive index mismatch between the solvent and particles restricts imaging only to the bottom layer.

Fig. 5 (A, top) shows measurements of the averaged boundary stress in the flow (σ_x) and vorticity (σ_y) directions for a time interval that includes the passage of three high stress events for the suspension of calcium carbonate particles. For comparison, in Fig. 5 (B, top), we have also depicted the corresponding outcomes for a suspension of adhesive cornstarch particles [47]. Both types of particles share a similar shape and polydispersity [42], so the differences between them are likely due to differences in particle interactions. This comparison can help us understand how interparticle attractions impact heterogeneities that arise during shear-thickening. In both suspensions, σ_x and σ_y exhibit similar time dependence although the latter has smaller magnitude. In the case of calcium carbonate suspensions, σ_y often exhibits slightly negative values at the initiation of the event. Additionally, for calcium carbonate suspensions, high-stress events occur nearly three times more frequently compared to cornstarch suspensions, which results in the formation of a well-defined low-stress region between consecutive high-stress events in the cornstarch suspension.

Fig. 5 (A, bottom) displays the velocities of the calcium carbonate particles at the bottom layer as determined by PIV, conducted concurrently with BSM. The fluctuations in velocity consistently coincide with periods of elevated boundary stress. Remarkably, during each event, the velocity in the flow direction (υ_x) exhibits an M-shaped profile, featuring two maxima and a minimum that coincides with the maximum in the boundary stress. The peculiar M-shaped variation of υ_x is also observed in suspensions of cornstarch particles (see Ref. [38] and Fig. 5 (B, bottom)). The velocity component in the vorticity direction (υ_y) for the calcium carbonate suspension shows variations that are much smaller than υ_x and difficult to distinguish from slow variations presumably unrelated to the passage of the high stress fronts. In contrast, the suspension of cornstarch particles shows significant variation of υ_y with an M-shape pattern similar to υ_x but with the smaller magnitude (Fig. 5 (B, bottom)).

In Fig. 6, we show the flow field recorded during the passage of one high stress region for the calcium carbonate particles at the bottom boundary. Away from the high stress event, particles exhibit predominantly affine low-speed flow (Fig. 6, i). As the event approaches, the speed increases rapidly in the flow direction (Fig. 6, ii). However, the flow in the vorticity direction is slightly directed towards the center of the rheometer's plate, as indicated by a slight negative value of υ_y. Moving further into the event, the speed in the flow direction decreases and reaches its minimum at the center of the event, where σ_x is maximized (Fig. 6, iii). However, the small positive values of υ_y observed

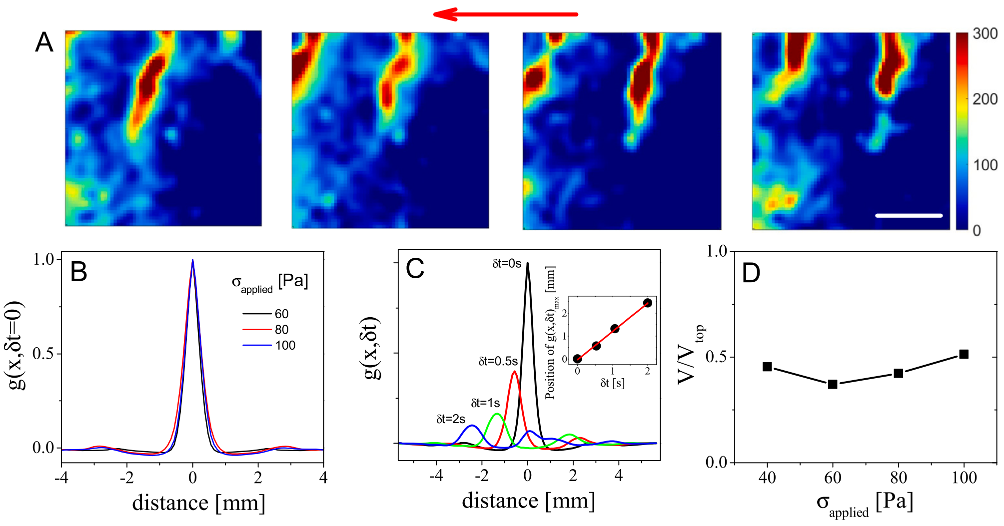

Fig. 4. (A) Snapshots of the boundary stress map in the flow direction (σ_x) captured at four consecutive time points under a constant applied shear stress of 100 Pa. The scale bar indicates a length of 2 mm, with the arrow indicating the direction of flow. (B) The normalized 2D autocorrelation of σ_x measured along the velocity direction at different values of applied stress. (C) The evolution $g(x, \delta t)$ at $\sigma = 100Pa$ for various lag times. Inset shows the shift in position of the $g(x, \delta t)$ peak as a function of lag time. (D) The propagation speeds of high-stress regions extracted from the slope of the inset, scaled by the speed of the rheometer's top boundary.

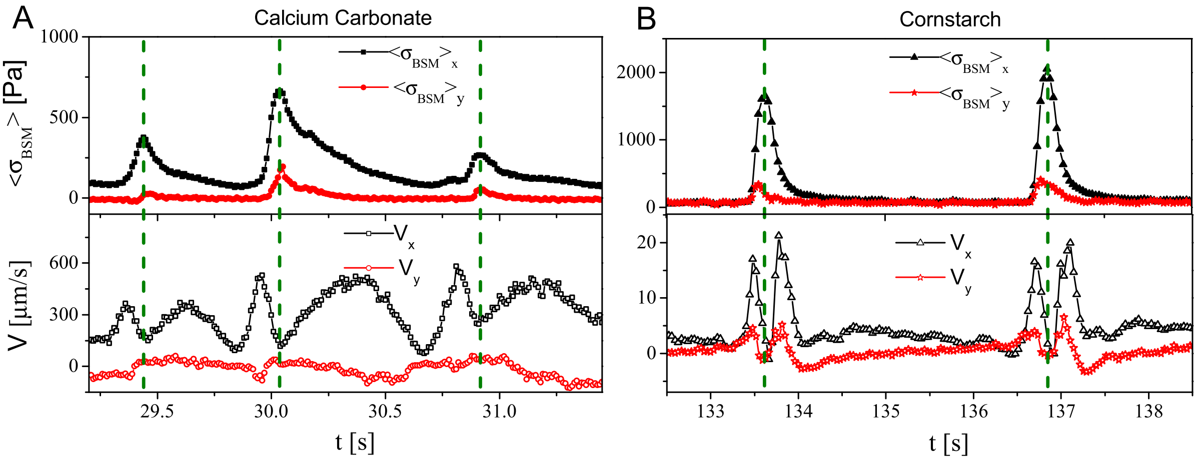

Fig. 5. (A, Top) Components of the boundary stress in the flow (x, filled black squares) and vorticity (y, filled red circles) directions. (A, Bottom) Components of the averaged velocity in the flow (x, open black squares) and vorticity (y, open red circles) directions for the suspension bottom layer. Dashed lines signify the time when the boundary stress attains its maximum value. Results in A are for the suspension of calcium carbonate particles with the applied stress of $150Pa$. Panel B is the same as A, but for a cornstarch suspension ($\phi_w = 42.3\%$) with the applied stress of $100Pa$ (see Ref. [38] for further details).

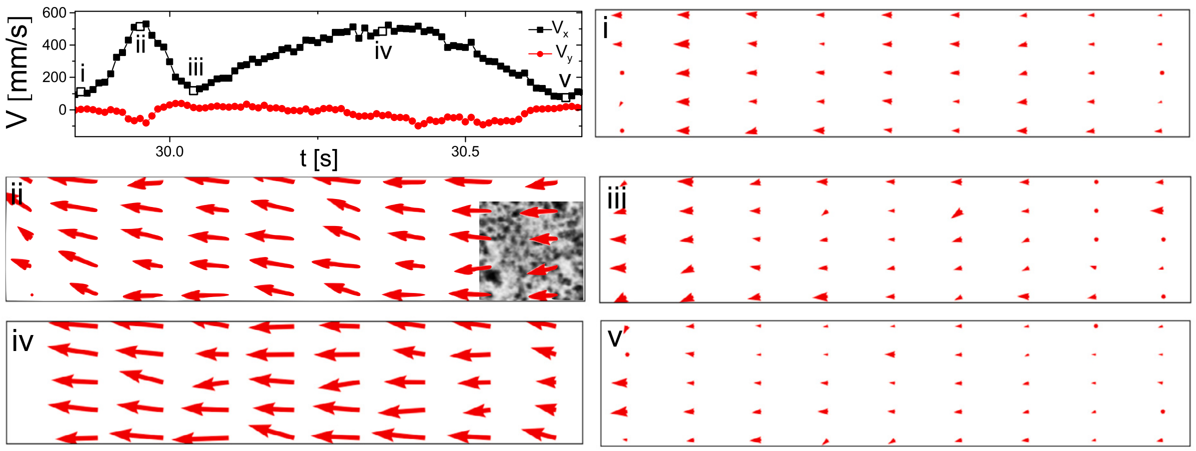

Fig. 6. The top left panel shows the components of the velocity for the second event in Fig. 5 (A, bottom). Images i to v display flow fields for calcium carbonate particles at specific time points, as shown by open squares on the plot of the average V_x in the Top Left panel. In (ii), we have shown part of the suspension. The full time variations of both the flow field and the boundary stress during the entire event are shown in Movie S2.

at this regime indicate a flow directed towards the outer boundary of the rheometer due to dilatant pressure, as discussed in [38]. Finally, the speed in the flow direction undergoes another acceleration (Fig. 6, iv) before eventually relaxing to a state of nearly affine flow (Fig. 6, v) at the back of the front. In Movie S2, we have shown the full time variations of both flow field and the boundary stress during the entire event.

5. Discussion

There is considerable evidence demonstrating that shear thickening in dense suspensions is closely linked to localized stresses, density fluctuations and non-affine motion [30,32,48,49,39,50–52,35–38,53,42,41]. Velocity measurements in a dense cornstarch suspension reveal the presence of localized velocity bands in the shear thickening regime, which propagate in the vorticity direction [41]. Moreover, in shear-thickening suspensions density waves that propagate in the direction of flow are also observed [32]. Both experiments and numerical simulations conducted on shear thickening systems clearly demonstrate the existence of dilatant fronts that propagate in the flow direction [52,50]. In our previous work on dense cornstarch suspensions [38], we observed that the dilatant pressure creates a localized region of direct frictional contact between particles and the boundary, accompanied by a significant transient flow in the vorticity direction.

Effects due to interparticle forces. The results reported here specifically highlight the impact of different interparticle forces. As mentioned earlier, both calcium carbonate and cornstarch particles share similar shapes and polydispersity. The main difference between the two suspensions lies in their interparticle interactions: in calcium carbonate suspensions, interactions are purely repulsive due to the added surfactant (PAA), whereas in cornstarch suspensions, attractive interactions are present [47]. As a consequence, the suspensions exhibit distinct rheological behaviors for stresses below shear thickening. Specifically, the calcium carbonate suspension shows a Newtonian response (Fig. 1A), while the cornstarch suspension shear-thins [42] as a result of the breakup of attraction-induced clusters [54].

When the applied stress is increased above the critical shear stress, both suspensions exhibit DST which we show is associated with localized regions of high stresses and an M-shaped pattern of nonaffine flows. However, there are clear differences between the two suspensions: (i) flow in the vorticity direction, which is likely an indication of dilatancy, is small in calcium carbonate suspensions (Fig. 5 (A, bottom)) whereas in cornstarch is significant (Fig. 5 (B, bottom)) and (ii) in cornstarch the speed of particles closest to the boundary at the center of the high-stress events reaches zero (Fig. 5 (B, bottom)) whereas in calcium carbonate suspensions the speed stays clearly above zero (Fig. 5 (A, bottom)). As discussed in [38], both the flow in the vorticity direction and the particle-boundary contact responsible for particle arrest at the boundary of the suspension can be attributed to the dilatant pressure arising from transient jamming. These two observations suggest that the dilatant pressure is smaller in calcium carbonate than in cornstarch, which is likely due to their difference in interparticle interactions. Additionally, in calcium carbonate suspensions, the high-stress fronts are notably unstable (Movie S1). This contrasts with adhesive cornstarch suspensions, where stable high-stress fronts are observed [38]. At a microscopic level, this distinction may stem directly from an enhancement of particle friction due to attraction [21,55,56], or from an increase in the temporal duration of contacts created by the propagating stress fronts.

Effects due to particle shape. The experimental results presented here, along with those from other systems, indicate that the general bulk rheological response and the stress inhomogeneity observed in the shear-thickening regime appear to be relatively insensitive to particle shape and interparticle forces [38,40,57]. However, the non-affine flow observed in high-stress regions significantly depends on particle shape. Particles with a rhomboid-like shape, such as calcium carbonate and cornstarch, exhibit a distinctive M-shaped velocity profile when high-stress fronts pass through. This characteristic is not observed in suspensions of silica microspheres [40].

We speculate that this phenomenon is a consequence of the increased impediments to rotation present in dense suspensions of rhomboidal particles relative to spheres. In the bulk, rhomboidal particles need more free volume to rotate, resulting in increased dilatant pressure in regions where contact networks are forming. Additionally, particles at the boundary align with their facets parallel to the flat surface [38]. This results in an increase of the overall contact area between the particles and surface, leading to a further reduction of the flow at the bottom of the dilatant front, which is the source of the velocity dip in the middle of the M-shaped non-affine flow. Finally, we note that additional rotation-resisting forces are present for rhomboid-like particles as a consequence of the dependence of interparticle interactions on relative particle orientation [58]. All of these effects are minimized or absent in spherical silica particles, which have a smaller contact area and greater freedom to rotate and pass each other.

Structure of propagating stress fronts. In this section, we discuss the mechanisms by which high-stress fronts form and propagate in the flow direction. Computational studies suggest that the rapid increase in viscosity within the DST regime arises from stress-induced frictional contacts [1,13–17]. Recent works suggest that a subset of mechanically rigid clusters within the frictional contact network is responsible for this viscosity increase [59,60]. Analysis of the particle contact network has revealed that fluctuations in large stresses are directly associated with the formation of a transient, percolated network of a specific subgroup of constrained particles [61]. We have proposed that these shear-jammed clusters, or solid-like phases (SLPs), are responsible for the experimentally observed localized high-stress regions and non-affine flows at the boundary [38].

While the front propagation speed is typically of the order of the boundary speed, the exact values show interesting variations that may shed light on the origin of high-stress regions. We have speculated that presence of a shear-jammed aggregate or SLP attached to the shearing plate will generate a high-friction fluid phase underneath that propagates with the top plate [57], and if there is material accretion ahead of the shear-jammed region, propagation speeds can exceed the speed of the top plate. In contrast, a shear jammed region that percolates between the top and bottom boundaries, with wall-slip at both boundaries, would lead to propagation rates of $\sim v_p/2$. This transition in propagation speed occurs sharply with changes in particle concentration or gap size [42]. At moderately high particle concentrations and large gaps, the propagation speed exceeds the top boundary speed. In contrast, as confinement increases either by reducing the gap or increasing particle concentration, the propagation speed drops to $v_p/2$, consistent with the hypothesis that the spatial extent of the shear jammed region increases with increasing particle concentration.

Contrast with measurements of local pressure. Direct measurements of local pressure at the millimeter scale in a shear-thickening suspension of cornstarch particles have shown localized regions of large pressures that propagate at a steady speed in the flow direction [53,42]. In contrast, suspensions of calcium carbonate particles, prepared identically to the suspensions studied here, did not show measurable pressure fluctuations [42]. The pressure measurements differ from the BSM measurements reported here in at least two important respects: BSM measures shear stress, as opposed to isotropic pressure, and our implementation of BSM has nearly micron scale spatial resolution, whereas the pressure sensors used in Ref. [42] average over an area of 4.5x4.5 mm^2. The spatial extent of the high stress regions detected by BSM is roughly the size of the 1 mm gap (Figs. 2 and 4), similar to measurements on suspensions of cornstarch [38] and silica microspheres [35,36], so the relatively large sensors used in Ref. [42] would be expected to measure a greatly reduced spatial variation, assuming the spatial extent of pressure heterogeneities is comparable to those of shear stress. Moreover, as mentioned above, the magnitude of pressure variation in calcium carbonate suspensions appears to be significantly smaller than those in cornstarch, adding to the detection challenge.

6. Conclusion

In conclusion, we have investigated the mechanism of shear-thickening in calcium carbonate suspensions by evaluating localized stresses and flow fields at the boundary. In general, shear thickening has been associated with fluctuations in bulk rheological properties such as viscosity and flow rate [27–32,35–38]. At the microscopic level, however, these fluctuations are found to be linked to localized stresses, density fluctuations, and nonaffine flows [30,32,48,49,39,50–52,35–38,40]. Nevertheless, a recent study investigating calcium carbonate suspensions with repulsive inter-particle interactions found no evidence of localized fluctuations at a millimeter scale using pressure sensors [42]. In contrast, cornstarch suspensions with sticky interactions have exhibited significant local pressure fluctuations in the shear-thickening regime [53,42]. This has raised the question of whether the mechanism governing shear thickening in a suspension is influenced by the nature of inter-particle interactions. To address this, we employed the BSM technique, capable of resolving stress inhomogeneities down to the particle level. Additionally, we monitored the flow field at the boundary where boundary stress is measured. We have identified localized regions of elevated stresses at the boundary for the calcium carbonate suspensions in the shear-thickening regime. These high-stress regions extend in the vorticity direction and propagate in the flow direction at a speed approximately one-half that of the rheometer's top plate. Notably, these regions of heightened stresses are found to play a pivotal role in the observed increase in viscosity with applied stress. Furthermore, the fluctuations observed in boundary stresses are accompanied by intricate nonaffine flows, displaying a distinctive shape similar to those observed in cornstarch suspensions [38]. Our work reveals a new aspect of shear thickening in calcium carbonate suspensions, namely, the emergence of stress and flow inhomogeneity. The findings presented herein, in conjunction with earlier investigations in shear-thickening suspensions [35–38,40,53], highlight that irrespective of the nature of interparticle interactions, a subtle interplay between localized stresses and nonaffine flows lies at the heart of the dramatic viscosity increase that characterizes shear thickening. A direct comparison between calcium carbonate and cornstarch suspensions reveals that the latter exhibits the formation of stable high-stress fronts, resulting in significant dilatancy, likely attributable to attraction-enhanced particle friction. Future research directions could explore systems where interparticle interactions are continuously adjusted (for example through depletion forces). This fine-tuning would enable a detailed examination of the impact of attractive interactions on both bulk response and local structure and dynamics. These investigations could be complemented by simulations involving large systems, realistic boundaries, and hydrodynamic models incorporating phenomena like shear jamming, dilatant pressure, and fluid migration.

CRediT authorship contribution statement

Esmaeel Moghimi: Writing – review & editing, Writing – original draft, Methodology, Investigation, Formal analysis, Data curation, Conceptualization. **Jeffrey S. Urbach:** Writing – review & editing, Writing – original draft, Supervision, Funding acquisition, Conceptualization. **Daniel L. Blair:** Writing – review & editing, Writing – original draft, Supervision, Funding acquisition, Conceptualization.

Declaration of competing interest

The authors declare that they have no known competing financial interests or personal relationships that could have appeared to influence the work reported in this paper.

Data availability

Data will be made available on request.

Acknowledgements

We thank Vikram Rathee and Joia Miller for providing data on cornstarch suspension. We also thank Emanuela Del Gado and Peter Olmsted for helpful discussions. This work was supported by the NSF under Grant 2226486.

Appendix A. Supplementary material

Supplementary material related to this article can be found online at https://doi.org/10.1016/j.jcis.2024.08.099.

References

[1] J.F. Morris, Shear thickening of concentrated suspensions: recent developments and relation to other phenomena, Annu. Rev. Fluid Mech. 52 (1) (2020) 121–144, https://doi.org/10.1146/annurev-fluid-010816-060128.

[2] N. Wagner, E.D. Wetzel, Advanced body armor utilizing shear thickening fluids, US Patent 7,498,276, Mar. 3, 2009.

[3] A. Majumdar, B.S. Butola, A. Srivastava, Optimal designing of soft body armour materials using shear thickening fluid, Mater. Des. (1980-2015) 46 (2013) 191–198.

[4] B.H. Manukonda, V.A. Chatterjee, S.K. Verma, D. Bhattacharjee, I. Biswas, S. Neogi, Rheology based design of shear thickening fluid for soft body armor applications, Period. Polytech., Chem. Eng. 64 (1) (2020) 75–84.

[5] T.H. Williams, J. Day, S. Pickard, Surgical and medical garments and materials incorporating shear thickening fluids, US Patent App. 12/440,086, Oct. 15, 2009.

[6] M. O'Leary, B. Hanson, C. Smith, Viscosity and non-Newtonian features of thickened fluids used for dysphagia therapy, J. Food Sci. 75 (6) (2010) E330–E338.

[7] J. Ding, W. Li, S.Z. Shen, Research and applications of shear thickening fluids, Recent Pat. Mater. Sci. 4 (1) (2011) 43–49.

[8] M. Zarei, M. Zarei, Self-propelled micro/nanomotors for sensing and environmental remediation, Small 14 (30) (2018) 1800912.

[9] S. Zhang, S. Wang, Y. Wang, X. Fan, L. Ding, S. Xuan, X. Gong, Conductive shear thickening gel/polyurethane sponge: a flexible human motion detection sensor with excellent safeguarding performance, Composites, Part A, Appl. Sci. Manuf. 112 (2018) 197–206.

[10] J.R. Melrose, R.C. Ball, "Contact networks" in continuously shear thickening colloids, J. Rheol. 48 (5) (2004) 961–978, https://doi.org/10.1122/1.1784784.

[11] D.R. Foss, J.F. Brady, Structure, diffusion and rheology of Brownian suspensions by Stokesian dynamics simulation, J. Fluid Mech. 407 (2000) 167–200, https://doi.org/10.1017/s0022112099007557.

[12] A.K. Gurnon, N.J. Wagner, Microstructure and rheology relationships for shear thickening colloidal dispersions, J. Fluid Mech. 769 (2015) 242–276, https://doi.org/10.1017/jfm.2015.128.

[13] M. Wyart, M. Cates, Discontinuous shear thickening without inertia in dense non-Brownian suspensions, Phys. Rev. Lett. 112 (9) (Mar. 2014), https://doi.org/10.1103/physrevlett.112.098302.

[14] M.E. Cates, M. Wyart, Granulation and bistability in non-Brownian suspensions, Rheol. Acta 53 (10–11) (2014) 755–764, https://doi.org/10.1007/s00397-014-0795-x.

[15] R. Mari, R. Seto, J.F. Morris, M.M. Denn, Discontinuous shear thickening in Brownian suspensions by dynamic simulation, Proc. Natl. Acad. Sci. 112 (50) (2015) 15326–15330, https://doi.org/10.1073/pnas.1515477112.

[16] N.Y. Lin, B.M. Guy, M. Hermes, C. Ness, J. Sun, W.C. Poon, I. Cohen, Hydrodynamic and contact contributions to continuous shear thickening in colloidal suspensions, Phys. Rev. Lett. 115 (22) (Nov. 2015), https://doi.org/10.1103/physrevlett.115.228304.

[17] E.Y.X. Ong, M. Ramaswamy, R. Niu, N.Y.C. Lin, A. Shetty, R.N. Zia, G.H. McKinley, I. Cohen, Stress decomposition in Laos of dense colloidal suspensions, J. Rheol. 64 (2) (2020) 343–351, https://doi.org/10.1122/1.5144520.

[18] L.C. Hsiao, S. Jamali, E. Glynos, P.F. Green, R.G. Larson, M.J. Solomon, Rheological state diagrams for rough colloids in shear flow, Phys. Rev. Lett. 119 (15) (2017) 158001.

[19] S. Pradeep, M. Nabizadeh, A.R. Jacob, S. Jamali, L.C. Hsiao, Jamming distance dictates colloidal shear thickening, Phys. Rev. Lett. 127 (15) (2021) 158002.

[20] C.-P. Hsu, S.N. Ramakrishna, M. Zanini, N.D. Spencer, L. Isa, Roughness-dependent tribology effects on discontinuous shear thickening, Proc. Natl. Acad. Sci. 115 (20) (2018) 5117–5122.

[21] C.-P. Hsu, J. Mandal, S.N. Ramakrishna, N.D. Spencer, L. Isa, Exploring the roles of roughness, friction and adhesion in discontinuous shear thickening by means of thermo-responsive particles, Nat. Commun. 12 (1) (2021) 1477.

[22] A. Singh, C. Ness, R. Seto, J.J. de Pablo, H.M. Jaeger, Shear thickening and jamming of dense suspensions: the "roll" of friction, Phys. Rev. Lett. 124 (24) (2020) 248005.

[23] B. Guy, M. Hermes, W. Poon, Towards a unified description of the rheology of hard-particle suspensions, Phys. Rev. Lett. 115 (8) (Aug. 2015), https://doi.org/10.1103/physrevlett.115.088304.

[24] J.R. Royer, D.L. Blair, S.D. Hudson, Rheological signature of frictional interactions in shear thickening suspensions, Phys. Rev. Lett. 116 (18) (May 2016), https://doi.org/10.1103/physrevlett.116.188301.

[25] C. Clavaud, A. Bérut, B. Metzger, Y. Forterre, Revealing the frictional transition in shear-thickening suspensions, Proc. Natl. Acad. Sci. 114 (20) (2017) 5147–5152, https://doi.org/10.1073/pnas.1703926114.

[26] J. Comtet, G. Chatté, A. Nigues, L. Bocquet, A. Siria, A. Colin, Pairwise frictional profile between particles determines discontinuous shear thickening transition in non-colloidal suspensions, Nat. Commun. 8 (1) (2017) 15633.

[27] D. Lootens, H. Van Damme, P. Hébraud, Giant stress fluctuations at the jamming transition, Phys. Rev. Lett. 90 (17) (Apr. 2003), https://doi.org/10.1103/physrevlett.90.178301.

[28] M. Grob, A. Zippelius, C. Heussinger, Rheological chaos of frictional grains, Phys. Rev. E 93 (3) (Mar. 2016), https://doi.org/10.1103/physreve.93.030901.

[29] A. Fall, F. Bertrand, D. Hautemayou, C. Mezière, P. Moucheront, A. Lemaître, G. Ovarlez, Macroscopic discontinuous shear thickening versus local shear jamming in cornstarch, Phys. Rev. Lett. 114 (9) (Mar. 2015), https://doi.org/10.1103/physrevlett.114.098301.

[30] J. Richards, J. Royer, B. Liebchen, B. Guy, W. Poon, Competing timescales lead to oscillations in shear-thickening suspensions, Phys. Rev. Lett. 123 (3) (Jul. 2019), https://doi.org/10.1103/physrevlett.123.038004.

[31] C. Ness, R. Mari, M.E. Cates, Shaken and stirred: random organization reduces viscosity and dissipation in granular suspensions, Sci. Adv. 4 (3) (Mar. 2018), https://doi.org/10.1126/sciadv.aar3296.

[32] G. Ovarlez, A. Vu Nguyen Le, W.J. Smit, A. Fall, R. Mari, G. Chatté, A. Colin, Density waves in shear-thickening suspensions, Sci. Adv. 6 (16) (2020) eaay5589.

[33] O. Sedes, A. Singh, J.F. Morris, Fluctuations at the onset of discontinuous shear thickening in a suspension, J. Rheol. 64 (2) (2020) 309–319.

[34] Q. Xu, A. Singh, H.M. Jaeger, Stress fluctuations and shear thickening in dense granular suspensions, J. Rheol. 64 (2) (2020) 321–328.

[35] V. Rathee, D.L. Blair, J.S. Urbach, Localized stress fluctuations drive shear thickening in dense suspensions, Proc. Natl. Acad. Sci. 114 (33) (2017) 8740–8745, https://doi.org/10.1073/pnas.1703871114.

[36] V. Rathee, D.L. Blair, J.S. Urbach, Localized transient jamming in discontinuous shear thickening, J. Rheol. 64 (2) (2020) 299–308, https://doi.org/10.1122/1.5145111.

[37] V. Rathee, D.L. Blair, J.S. Urbach, Dynamics and memory of boundary stresses in discontinuous shear thickening suspensions during oscillatory shear, Soft Matter 17 (5) (2021) 1337–1345, https://doi.org/10.1039/d0sm01917h.

[38] V. Rathee, J. Miller, D.L. Blair, J.S. Urbach, Structure of propagating high-stress fronts in a shear-thickening suspension, Proc. Natl. Acad. Sci. 119 (32) (2022) e2203795119.

[39] W.H. Boersma, P.J.M. Baets, J. Laven, H.N. Stein, Time-dependent behavior and wall slip in concentrated shear thickening dispersions, J. Rheol. 35 (6) (1991) 1093–1120, https://doi.org/10.1122/1.550167.

[40] J.M. Miller, D.L. Blair, J.S. Urbach, Order and density fluctuations near the boundary in sheared dense suspensions, Front. Phys. 10 (Nov. 2022), https://doi.org/10.3389/fphy.2022.991540.

[41] B. Saint-Michel, T. Gibaud, S. Manneville, Uncovering instabilities in the spatiotemporal dynamics of a shear-thickening cornstarch suspension, Phys. Rev. X 8 (3) (Jul. 2018), https://doi.org/10.1103/physrevx.8.031006.

[42] A. Gauthier, G. Ovarlez, A. Colin, Shear thickening in presence of adhesive contact forces: the singularity of cornstarch, J. Colloid Interface Sci. 650 (2023) 1105–1112, https://doi.org/10.1016/j.jcis.2023.07.017.

[43] J.A. Richards, R.E. O'Neill, W.C.K. Poon, Turning a yield-stress calcite suspension into a shear-thickening one by tuning inter-particle friction, Rheol. Acta 60 (2–3) (2020) 97–106, https://doi.org/10.1007/s00397-020-01247-z.

[44] S.K. Dutta, A. Mbi, R.C. Arevalo, D.L. Blair, Development of a confocal rheometer for soft and biological materials, Rev. Sci. Instrum. 84 (6) (Jun. 2013), https://doi.org/10.1063/1.4810015.

[45] R.W. Style, R. Boltyanskiy, G.K. German, C. Hyland, C.W. MacMinn, A.F. Mertz, L.A. Wilen, Y. Xu, E.R. Dufresne, Traction force microscopy in physics and biology, Soft Matter 10 (23) (2014) 4047, https://doi.org/10.1039/c4sm00264d.

[46] H.A. Barnes, Shear-thickening ("dilatancy") in suspensions of nonaggregating solid particles dispersed in Newtonian liquids, J. Rheol. 33 (2) (1989) 329–366, https://doi.org/10.1122/1.550017.

[47] L. Oyarte Gálvez, S. de Beer, D. van der Meer, A. Pons, Dramatic effect of fluid chemistry on cornstarch suspensions: linking particle interactions to macroscopic rheology, Phys. Rev. E 95 (3) (2017) 030602.

[48] A. Fall, F. Bertrand, G. Ovarlez, D. Bonn, Shear thickening of cornstarch suspensions, J. Rheol. 56 (3) (2012) 575–591, https://doi.org/10.1122/1.3696875.

[49] M. Hermes, B.M. Guy, W.C.K. Poon, G. Poy, M.E. Cates, M. Wyart, Unsteady flow and particle migration in dense, non-Brownian suspensions, J. Rheol. 60 (5) (2016) 905–916, https://doi.org/10.1122/1.4953814.

[50] H. Nakanishi, S.-i. Nagahiro, N. Mitarai, Fluid dynamics of dilatant fluids, Phys. Rev. E 85 (1) (Jan. 2012), https://doi.org/10.1103/physreve.85.011401.

[51] R.J. Larsen, J.-W. Kim, C.F. Zukoski, D.A. Weitz, Fluctuations in flow produced by competition between apparent wall slip and dilatancy, Rheol. Acta 53 (4) (2014) 333–347, https://doi.org/10.1007/s00397-014-0764-4.

[52] S.-i. Nagahiro, H. Nakanishi, Negative pressure in shear thickening band of a dilatant fluid, Phys. Rev. E 94 (6) (Dec. 2016), https://doi.org/10.1103/physreve.94.062614.

[53] A. Gauthier, M. Pruvost, O. Gamache, A. Colin, A new pressure sensor array for normal stress measurement in complex fluids, J. Rheol. 65 (4) (2021) 583–594, https://doi.org/10.1122/8.0000249.

[54] D.B. Genovese, Shear rheology of hard-sphere, dispersed, and aggregated suspensions, and filler-matrix composites, Adv. Colloid Interface Sci. 171 (2012) 1–16.

[55] B. van der Meer, T. Yanagishima, R. Dullens, Emergence of interparticle friction in attractive colloidal matter, arXiv preprint, arXiv:2209.12703, 2022.

[56] N. Park, V. Rathee, D.L. Blair, J.C. Conrad, Contact networks enhance shear thickening in attractive colloid-polymer mixtures, Phys. Rev. Lett. 122 (22) (2019) 228003.

[57] V. Rathee, S. Arora, D.L. Blair, J.S. Urbach, A. Sood, R. Ganapathy, Role of particle orientational order during shear thickening in suspensions of colloidal rods, Phys. Rev. E 101 (4) (2020) 040601.

[58] J. Lee, E. Nakouzi, J. Heo, B.A. Legg, G.K. Schenter, D. Li, C. Park, H. Ma, J. Chun, Effects of particle shape and surface roughness on van der Waals interactions and coupling to dynamics in nanocrystals, J. Colloid Interface Sci. 652 (2023) 1974–1983.

[59] M. van der Naald, A. Singh, T.T. Eid, K. Tang, J.J. de Pablo, H.M. Jaeger, Minimally rigid clusters in dense suspension flow, Nat. Phys. (2024) 1–7.

[60] A. Santra, M. Orsi, B. Chakraborty, J.F. Morris, Rigid clusters in shear-thickening suspensions: a nonequilibrium critical transition, arXiv preprint, arXiv:2401.15165, 2024.

[61] A. Goyal, N.S. Martys, E. Del Gado, Flow induced rigidity percolation in shear thickening suspensions, J. Rheol. 68 (2) (2024) 219–228.